Lawrence Berkeley National Laboratory

Title
Solid 3D Li–S Battery Design via Stacking 2D Conductive Microporous Coordination Polymers and Amorphous Li–S Layers

Permalink
https://escholarship.org/uc/item/8db9s3cv

Authors
Gao, Guoping
Zheng, Fan
Wang, Lin-Wang

A solid 3D Li-S battery design via stacking 2D conductive microporous coordination polymers and amorphous Li-S layers

Guoping Gao, Fan Zheng, Lin-Wang Wang*

Materials Sciences Division, Lawrence Berkeley National Laboratory, Berkeley, California 94720, USA. E-mail: lwwang@lbl.gov

Abstract

In order to make a Li-S battery practical, not only high gravimetric energy capacity is important, high volumetric energy capacity will also be required. The currently explored Li-S cathode designs often deploy systems with liquid electrolyte infiltration, hence with relatively low volumetric capacity. In the current study, we theoretically test a compact solid 3D design (more like a Li-ion battery cathode than a conventional Li-S cathode) consisted of a sandwich structure alternating between the 2D Mn-hexaaminobenzene-based coordination polymers (2D Mn-HAB-CP) layer and amorphous Li-S layer. We study the theoretical limits for both its gravimetric and volumetric energy capacity, as well as its structural stability and Li diffusion within the cathode system. In order to study the Li diffusion within an amorphous system, we also develop a pull-atom molecular dynamics (PA-MD) to calculate the barrier heights of such disordered systems. We reveal the mechanism which determines the Li diffusion in the amorphous layer of the system. Overall, we find such 3D solid Li-S cathode can be practical, with sufficient large gravimetric and volumetric energy capacity, as well as the Li diffusion constant. It also solves many other common Li-S cathode problems, from Li polysulfide dissolution to electrical insulating, and structure instabilities.

Introduction

Li-S battery that coupled natural-abundant and environmental friendliness sulfur positive electrodes (cathodes) with lithium negative electrodes (anodes) is regarded as a promising next-generation electrochemical energy storage system due to its potential of high density gravimetric and volumetric energy storages (2600 Wh/kg and 2800 Wh/L) at low cost[1]. However, the insulating nature of sulfur and the solid-state reduction products (Li_2S_2 and Li_2S) limit the sulfur utilization[2]. Furthermore, the soluble intermediate polysulfide species produced from the cathode can migrate through the liquid electrolyte to react with lithium on the anode, resulting in fast capacity fading, low Coulombic efficiency, and poor cycle life[3]. In practice, there is a dilemma between the insulating nature of the bulk sulfur and the adverse effects of polysulfide dissolution. On the one hand, to overcome the insulating nature of the bulk sulfur, it is necessary to dissolve the intermediate polysulfide species, so the discharging process can be completed. On the other hand, the dissolution can cause all the problems mentioned above. This calls for new cathode designs beyond the simple bulk sulfur electrode. In addition, the large volume change (80%) during the cycling process taking place in sulfur cathodes can cause structural damage and mechanical instability[4].

To address the above problems, the research community has worked on novel Li-S cathode materials and designs. Infiltrating molten sulfur into porous conductive carbon materials has

improved the capacities and cycle lives of Li–S batteries[5]. However, merely spatially encaging the lithium polysulfide (LiPS) by carbon is not sufficient to suppress it diffusion[3]. To address this issue, sulfur host materials with strong chemical binding with LiPS, such as graphene oxides[6], graphene nitride[7], functional polymeric binder[8], are investigated to prevent LiPS from dissolution thermodynamically. Metal-organic framework (MOF), with metal atoms to realize stronger binding with LiPSs, high surface area, and tunable porosity, can potentially suppress the LiPS diffusion as well as alleviates the volume change during the cycling process[9]. However, their low electrical conductivity is a major shortcoming, as well as the structural stability. Recently, a new class of conductive two-dimensional metal-organic frameworks: 2D hexaaminobenzene based coordination polymers (2D-HAB-CPs), has been synthesized[10], and are proven to be a high-performing electrode with exceptionally high volumetric and areal capacitance[11]. In addition, these materials also exhibit excellent chemical stability in both acidic and basic aqueous solutions, which allows for their use in low-cost and non-flammable aqueous electrolytes. These characters make HAB-CPs a potential cathode material for Li-S battery.

All the above designs, either sulfur in porous carbon materials, or LiPS chemical binding with 2D films or polymer binders, depend on the intrusion of liquid electrolyte directly inside the cathode, or in touch with the surface of 2D films. Such designs can suffer from the low volumetric capacity. For example, the gravimetric energy density of Li-S battery developed by OXIS Energy Ltd has achieved 400 Wh/kg in practice and is expected to reach 500 Wh/kg in near future, which is twice that of the state-of-the-art lithium-ion batteries (LIBs)[12]. However, its volumetric energy density (~330 Wh/L) is far less than that of LIBs[13]. In order to make a Li-S battery practical, a surface sulfur loading of 5 mg/cm^2 will be necessary[14]. For the 2D-HAB-CPs systems mentioned above[15], this corresponds to ~50000 layers of materials. It is difficult to reach this goal if only loose 2D flakes are submerged in liquid electrolytes. One important question is then: whether it is possible to design a solid 3D Li-S cathode, which retains the strong binding between Li and S atoms, hence the high gravimetric energy density, but also has the spatial compactness of a 3D solid, thus will also have the high volumetric capacity. Such a compact design will necessarily extrude the liquid electrolyte outside the cathode and involve quasi-solid state reactions during the lithiation as observed in ultramicroporous carbon systems[15], therefore avoiding the dissolution of polysulfides. However, the ability of the Li-ion diffusing inside the 3D cathode becomes critical. Since Li-S forms a weak covalent bond, the Li diffusion inside such a 3D material involves the breaking and forming of such covalent bonds in strong contrast of LIBs in which intercalation is the main binding mechanism. It is thus doubtful whether the Li-ion in such a cathode can be mobile at all. In the design of such 3D sulfur electrode, one might attempt to find some 3D crystal structures. However, most such crystal structures have their S already bonded with other cations, thus it is difficult to change their valence states and to bind additionally Li (e.g., in many sulfide-based solid electrolyte)[16]. One approach is to keep the nature of LiPS, which is to exchange between the S-S bond and Li-S bond during the lithiation process. In practice, this might involve S-S chains or clusters, thus it is likely an amorphous structure. Another concern is the volume expansion of such a system after lithiation. It is important to keep the volume expansion under a few percent in order to have a good mechanical stability of the battery. Finally, the electrical conductivity inside the 3D structure is always critical.

In this work, we propose a 3D Li-S battery cathode design. This is based on the 2D-HAB-CP material studied in our previous work[17]. Here, instead of having only one layer of 2D-HAB-CP with Li-S cluster anchored on the surface, we design a 3D sandwiches structure with alternating 2D-HAB-CP layer and Li-S amorphous layers as shown in Fig.1. The binding of the S or Li-S cluster to the transition metal in 2D-HAB-CP layer helps to stabilize the 3D structure, and also prevent the Li-S from aggregating into isolated chunks. As shown in our previous work[17], the chemical binding strength of Li-S to the 2D layer is just strong enough to prevent their dissolution thermodynamically. In the new 3D design, this aspect is further improved by the physical confinement of the Li-S within the sandwich layers. The electrical conductivity of 2D-HAB-CP framework guarantees the whole electrode is conductive. The binding between Li-S basically keeps the original nature of LiPS, it can thus provide high gravimetric capacity. There are two challenges to theoretical study the proposed system: (1) structure stability during lithiation; and (2) Li diffusivity inside such an amorphous material. For the first challenge, we have used our genetic algorithm searching approach which is also used in our previous study[17]. Here, in searching the Li-S structure within the layer of 2D-HAB-CP, we have fixed the 2D-HAB-CP layer while using a mating algorithm to generate the new configurations of the amorphous Li-S structure. The detail is described in Fig.S1. Li diffusion can be calculated in several approaches. The direct approach is via *ab initio* molecular dynamics (MD), thus the diffusion distance square as a linear function of the time will give us the diffusion coefficient as the slope of the linear curve[18]. However, this method will only work when the diffusion constant is relatively high like in solid electrolyte, so MD with a few picoseconds will be sufficient to observe the diffusion. In some systems (e.g., solid electrolyte), one can use higher temperatures to accelerating the diffusion, and using Arrhenius's law to extrapolate to low-temperature diffusion (assuming only one diffusion barrier play an important role throughout the temperature range)[18]. Unfortunately, in our system, too high temperature can melt our system, causing a phase transition into another state. Another common approach is to use the nudged elastic band (NEB) method to calculate the diffusion barrier height[19]. This, however, is only practical when the minimum energy atomic configures before and after the transition are known. This is thus often used for crystal systems where the path of the Li diffusion is already known. A more general method is kinetic Monte Carlo (MC) method with on-the-fly generation of transition path using dimmer method to explore all possible transition path[20]. While this is more robust, it is also more time consuming and requires the set-up of a major workflow framework. In a constrained MD, a geometric constraint (e.g., distance between two atoms, or simply the position of an atom) is enforced by an additional Lagrangian multiplier. The amplitude of this multiplier (λ) is solved every step in the MD to ensure the MD trajectory will satisfy the constraint(reference?). Usually, the force related to this constraint, not the force on the surrounding atoms, is used to carry out some thermal dynamical integration to get the free energy difference between two states where two different constraints exist. It assumes the surrounding atoms (e.g., solvent molecules) reach an equilibrium. In a solid, the surrounding atoms certainly do not reach a true thermal dynamic equilibrium. Therefore, it is not clear whether one can use constrained MD to reveal the barrier height. Finally, one can use a metadynamics to estimate the free energy along a given reaction path[21]. However, for an amorphous system which is homogeneous in an average sense, it could be difficult to sample the reaction path to get the barrier height. In the current study, we propose a new dynamics method (to be called pull-atom molecule dynamics, PA-MD), where an external artificial force is applied to one atom (Li), to

force it to move along a direction. A local thermostat is applied to the atom, so it will have sufficient random kinetic energy to explore the local environment, while keeping the other atoms in the system cool (to reduce the statistical noise, and to prevent the whole system from melting). The potential energy of the system along the MD trajectory is then analyzed to reveal the barrier height. We will show that this method allows us to estimate the diffusion barrier height. In a simple case like solid crystal, it yields the same result as the NEB method. We believe this approach can also be used to study other amorphous systems.

Our theoretical study can provide answers to whether such a compact 3D system design direction is a good approach for Li-S cathode design, and what are the main challenges in such design. Through our theoretical calculation, we found that depending on the degree of lithiation, the Z-direction interlayer distance can change from a few percent to 20%. The Li mobility inside the material, although much less than that of LIB materials like LiNiMnCoO (NMC_{523} and NMC_{333}), it can be better than other Li cathodes like $LiFePO_4$, and similar to $LiNi_{0.5}Mn_{1.5}O_4$ and even close to some of the solid electrolytes, e.g. LLZO[22]. Overall, our study indicates that such compact 3D Li-S cathode could be practical.

Computational details

All calculations were performed using planewave DFT calculations implemented in the PWmat code[23] with norm-conserving pseudopotential. The exchange-correlation interactions were treated by the generalized gradient approximation in the form of the Perdew–Burke–Ernzerhof functional[24]. The Van der Waals interaction was described by using the empirical correction in Grimme's scheme, i.e. DFT+D2[25]. The spin=2 polarization was used in all the calculations. The electron wave functions were expanded by plane waves with cut-off energies of 680 eV, and the convergence tolerance for residual force and energy on each atom during structure relaxation were set to 0.005 eV Å^{-1} and 10^{-5} eV, respectively. The Hubbard U (DFT+U) treatment was used on the transition metal. The U value for Mn was set to 3.06 eV following the literature value[26].

The structure of the system is designed by stacking up 2D Mn-HAB monolayers, while inserting Li_xS_8 between the layers. We treat Z-direction (stacking direction) as periodic. One unit cell of 2D Mn-HAB (one hole in Fig.1 (a), or say 3 Mn atoms) will have one Li_xS_8. To yield the atomic configuration of the system for a given Li_xS_8 (x ranges from 5 to 20), we have used genetic algorithm scheme to search the possible structures. An in-house code is used which implements the genetic algorithm to find the global minimum[27]. The process of our global minimum structure search method is present in Figure S1 in the Supporting Information. To evaluate the volume expansion, we assume the lattice parameter in X- and Y-axis are constant, which is determined by the lattice constant of 2D Mn-HAB, and adjust Z-axis value manually in the global minimum structures search to obtain the most energy-favorable Z-lattice value as shown in the figure 1. Therefore the volume expansion can be obtained by comparing the Z-lattice values in different discharge stages.

In order to calculate the energy density during the lithiation process, it is necessary to calculate the formation energy of different intermediate species as the following:

$$E_{form} = E_{Li_xS_8 \, on \, Mn-HAB} - E_{S_8-Mn-HAB} - xE_{Li \, bulk \, per \, atom} \quad (1)$$

Here, $E_{Li_xS_8 \, on \, Mn-HAB}$, and $E_{S_8-Mn-HAB}$ are the total energy of Li_xS_8 on Mn-HAB, and S_8 on Mn-HAB, respectively. $E_{Li \, bulk \, per \, atom}$ is the energy per Li atom in its bulk form. The gravimetric energy density and volumetric energy density is calculated by equation (2) and (3), respectively:

$$E_{gravimetric \, energy \, density} = E_{form}/m \quad (2)$$

$$E_{volumetric \, energy \, density} = E_{form}/V \quad (3)$$

Here, m and V is only the mass and volume of cathode materials Li_xS_8-Mn-HAB but does not consider the mass and volume of other parts of the battery, respectively.

To calculate the diffusion constant, we use a 3D random walk formula [28] as following:

$$D = \frac{d^2}{6\tau} \qquad\qquad (4)$$

Where, d is the average jump length and τ is the average jumping time which is expressed as:

$$\frac{1}{\tau} = ve^{-\Delta E/k_BT} \qquad\qquad (5)$$

Where v is the effective frequency of the jumping atom. This v is estimated by the oscillation frequency of Li towards the direction of the hopping. $ve^{-\Delta E/k_BT}$ is jump rates governed by the Arrhenius expression. ΔE is the average migration barrier of Li, which will be calculated later by our special AP-MD in the NVT ensemble. Therefore, equation 4 can be written in the following form:

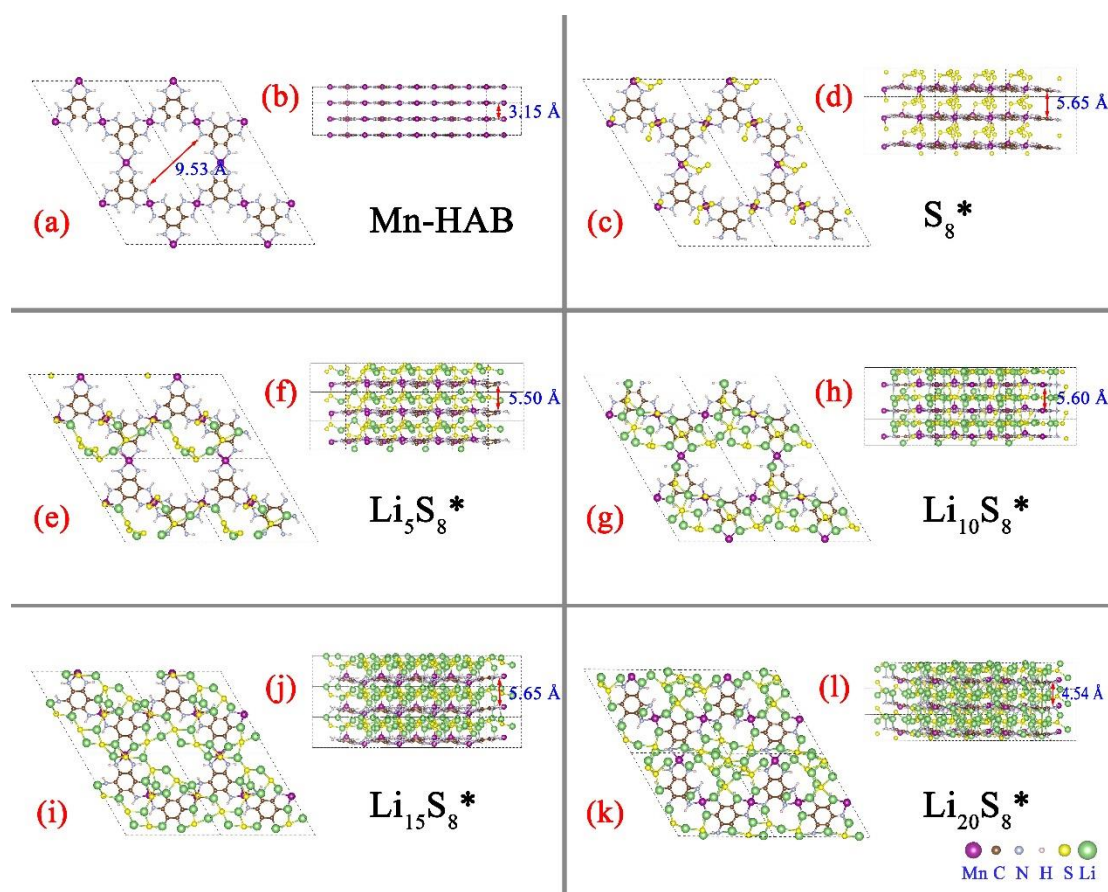$$D = \frac{d^2ve^{-\Delta E/k_BT}}{6} \qquad\qquad (6)$$

Results

Figure 1 the top view and side view of 3D Mn-HAB, and S_8, Li_5S_8, $Li_{10}S_8$, $Li_{15}S_8$ and $Li_{20}S_8$ in this fabrication. The * represents the Mn-HAB. The bond length cut-off for Mn-S is 2.4 Å, for N-Li is 2.4 Å, for S-S is 2.4Å, for Li-S is 2.6 Å, and for possible Mn-Li is 2.6 Å.

We first show the structural and thermodynamics results before discussing our new procedure to calculate the barrier height in an amorphous system. Fig 1a presents the structures of layer-by-layer 3D Mn-HAB fabrication with a honeycomb lattice. The interlayer spacing is 3.15 Å. The pores with a diameter of 9.53 Å are vertically aligned and uniformly distributed in the 3D Mn-HAB system. The global minimum locations for S_8, Li_5S_8, $Li_{10}S_8$, $Li_{15}S_8$, and $Li_{20}S_8$ between Mn-HAB layers are searched through an in-house developed genetic algorithm code to simulate the molecule sulfur and lithiation processes. Their configurations are shown in Fig. 1c -1l. With the one S_8 molecule per unit cell, the strong interaction between Mn and sulfur breaks the S_8 molecule into one S_2 and two S_3 chains, which indicate the Mn-HAB can capture and activate the insulating S_8 efficiently. Meanwhile, these short S chains dramatically increase the interlayer distance from 3.15 Å to 5.65 Å. At early lithiation stages (5 and 10 Li atoms per unit), the Li atoms break S-S bonds into isolated S atoms. As a result, there are 1D horizontal wires grow along the edge of pores with a few Li-S bonds forming vertically in the pores to connect the 1D wires. Meanwhile, these wires bind on the Mn-HAB through Mn-S bonds and Li-N bonds to stabilize the Li_5S_8 and $Li_{10}S_8$ clusters in the system. The important roles of Mn-S bonds and Li-N bonds at early discharge stage can be confirmed by the enlarge view of Li_5S_8* as shown in the Fig S2a, supporting information, in which the Li_5S_8 cluster binds on the Mn-HAB through these two kinds of bonds. When the Li density increases (15 Li atoms and 20 Li atoms per unit), the coordination

numbers of S atoms are increased to 4 or more (see Table 1). The Li-S bonds inhabit the Mn-S bonds and the S atoms are terminated by lithium atoms only. Meanwhile, the 1D Li_xS_8 wires interweave into a 2D structure between the Mn-HAB layers, with some of the Li atoms binding firmly on the nitrogen atoms in the Mn-HAB as shown in the enlarged views of $Li_{20}S_8$* (Fig S2b, supporting information), in which no Mn-S bonds are found. with 15 Li atoms, the volume change of the system upon lithiation is less than 2.65% relative to the S_8-Mn-HAB. When the Li density is increased furtherly to 20 Li atoms per unit, a Li-S Pillar covered by Li atoms forms in the pore of Mn-HAB, and surprisingly the interlayer spacing shrinking to 4.54 Å. This shrink of interlayer distance with more Li is due to the moving of Li-S towards the vertical hole region, thus depleting the Li-S between the layer. This formation of Li-S pillar is only possible with sufficient Li atoms to connect the Li-S between different layers. Based on our calculation, the LiPSs are amorphous rather than in periodic atomic arrangement during the lithiation. Such amorphous structures could be more active than the crystalline ones, as observed experimentally[29]. In the early stage of the lithiation process, the coordination number of S to Li atoms is relatively low, thus Mn-S binding is critical to stabilize LiPS into the solution. At the end stage of lithiation, Li-N bond plays an important role in anchoring LiPS to the Mn-HAB framework.

Table 1 the number of S atoms with different Li-S bonds (per S atom) coordinations at different lithiation stages. The Li-S bonds of every S atom are counted with a cut-off distance of 2.60 Å.

Coordination Number	Li_5S_8*	$Li_{10}S_8$*	$Li_{15}S_8$*	$Li_{20}S_8$*
0	1			
1	3	1		
2	3	2		
3	1	3		1
4		1	7	2
5		1	1	
6				4
7				1

Figure 2 plots the gravimetric energy density of Li_xS_8 on Mn-HAB as a function of the number of Li (the dash-dot line). During the initial lithiation process (Li_5S_8-$Li_{10}S_8$), the gravimetric energy density slop is small due to difficulty in activating the insulating S. Then slop increases during the period ($Li_{10}S_8$-$Li_{15}S_8$), followed by a slight tapering ($Li_{15}S_8$-$Li_{20}S_8$). The tapering occurs when the S atoms are saturated gradually. The total gravimetric energy density of $Li_{20}S_8$ on Mn-HAB is 825 Wh/Kg. This gravimetric energy density is slightly smaller than what is available in 2D Mn-HAB (1012 Wh/Kg)[17]. The volumetric energy density of Li_xS_8 on the Mn-HAB at different lithiation stages are shown as the pillars in Figure 2. The volumetric energy density is 297 Wh/L with only five lithium added (Li_5S_8). With ten lithium added, the volumetric energy density is 586 Wh/L. The volumetric energy density increase to 1076 Wh/L when Mn-HAB loaded with $Li_{15}S_8$. The value further reaches to 1652 Wh/L if Mn-HAB fully loaded (Mn-HAB-$Li_{20}S_8$), which is about 5 times of the state-of-the-art Li-S value obtained by OXIS Energy Ltd[12a]. Therefore, the layer-by-layer 3D Mn-HAB design will sacrifice the gravimetric energy density compared to the single-layer 2D structure, but it will boost the volumetric energy density to an extremely high value.
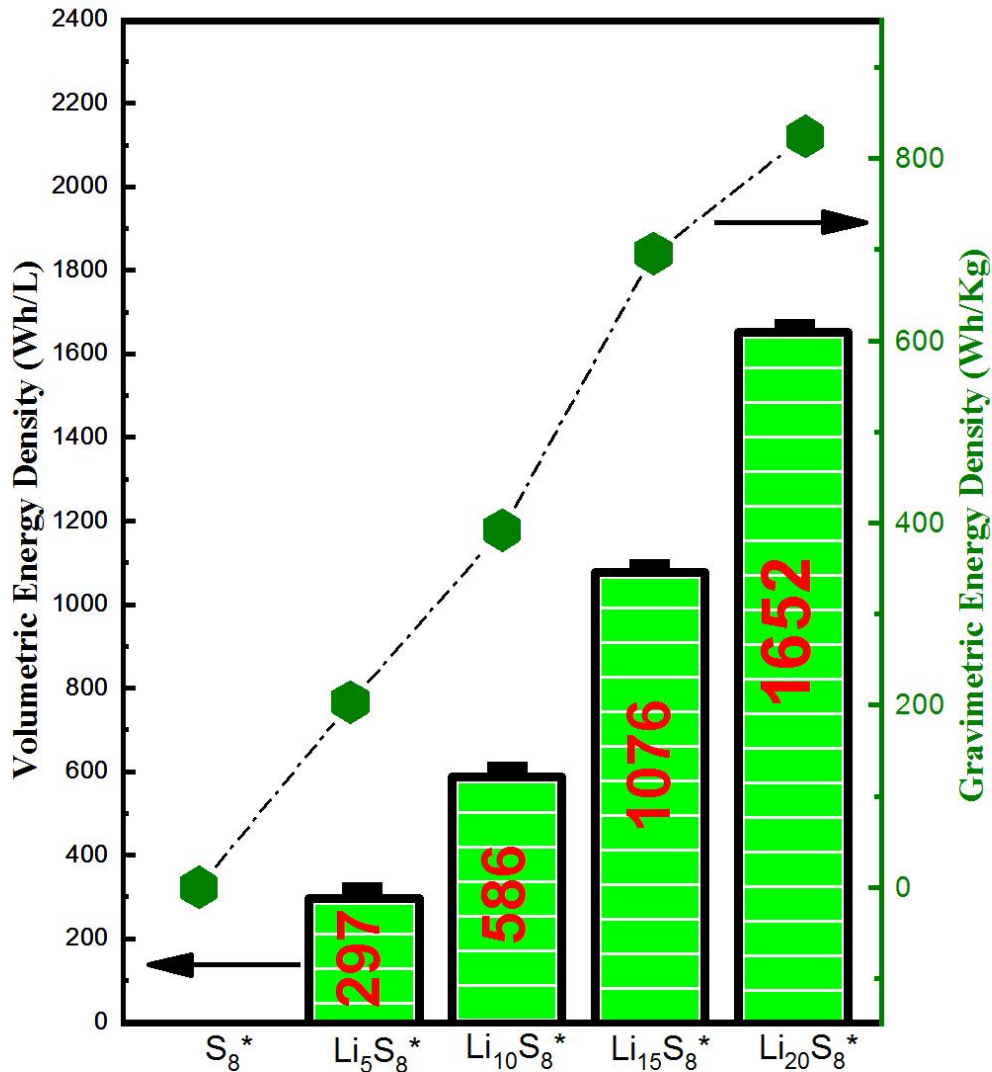
Figure 2 the gravimetric energy density per Li_xS_8 unit on Mn-HAB (right side vertical axis), and the corresponding volumetric energy density (pillars) as a function of the number of Li.

For battery charge and discharge to occur, there must be a concurrent transfer of both electrons and ions. The electrical conductivity can be estimated by the band structure of electrodes materials from our calculations. We show that there is no band gap found from Mn-HAB, S_8-Mn-HAB to $Li_{15}S_8$-Mn-HAB, and only a very small electron band gap is found at the end of lithiation (0.09 eV in $Li_{20}S_8$'s case) as shown in Figure S3, supporting information. We expect the system displays excellent electrical conductivity for efficient lithiation.

Now, we will turn to the study of Li diffusion in the system. Since there is no liquid electrolyte infiltration, the Li has to be able to diffuse in the system in order to realize the lithiation process. This could be a general issue for any compact solid-state Li-S cathode design without liquid electrolyte infiltration. Since the system is amorphous, and the diffusion is relatively slow (for direct *ab initio* molecular dynamics simulation), the estimation of the diffusion constant is

challenging. All the conventional methods of *ab initio* diffusion constant calculations mentioned above are not applicable to the current problem. In the following, we design a new approach to estimate the Li-ion diffusion in amorphous systems. In this approach, one atom (a Li atom) is subject to an artificial external force. Besides this external force, a special Langevin dynamics is designed, with the equation:

$$m_i \ddot{R}_i = F_i - \gamma_i v_i + R_i(t) = m_i a_i \quad (7)$$

here, $\gamma_i v_i$ is the frictional force, and $R_i(t)$ is the random force. In our special Langevin algorithm, while all the atoms have the dissipation force with γ_i equals 0.5 eV*fs/ Å^2, only the Li atom with external pull force has the random force $R_i(t)$ corresponds to 300K temperature in a normal Langevin algorithm, while this random force is zero for all the other atoms. This will effectively heat up this Li atom, while the temperature will gradually cool down away from this Li atom. The local heating will allow this Li atom to effectively search for minimum transition path under the pulling force, while the near-zero temperature for atoms far away can avoid the melting of the whole system, and to reduce the statistical random noise in the potential energy along the trajectory.
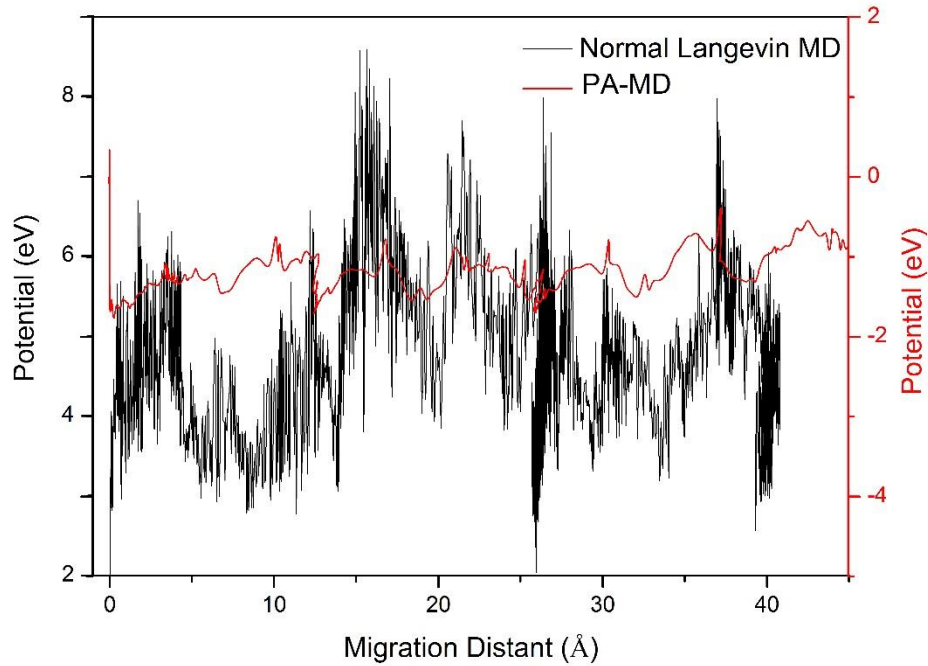

Figure 3. With an external force (0.5 eV/Å in the X-direction) applied to a targeted Li, the potential evolutions of 3D Mn-HAB-Li$_5$S$_8$ system via normal Langevin MD (black line) and Langevin PA-MD with other atoms specified at 0K (red line).

.

We will first use Mn-HAB-Li$_5$S$_8$ as an example to illustrate this method. The potential energy evolution (the DFT total energy, without the nuclear kinetic energy) of the whole 3D Mn-HAB-Li$_5$S$_8$ system (with 104 atoms) as a function of the Li migration distance when one Li is under an external force (0.5 eV/Å in the X-direction) in a normal Langevin MD is shown as the black line in Fig.3, while our special Langevin MD result is shown as the red line. As we can see,

the potential fluctuates dramatically with large amplitudes due to the random movement of all the atoms in the normal MD. While the fluctuation of the special Langevin dynamics with a local thermostat is much smaller. The amplitude of the random force on that pull atom is adjusted so that the measured nuclear kinetic energy for the pulled atom corresponds to 300K. After this procedure, the pulled atom will jump from one location to another, and the total potential energy shows clear bumps from time to time. We like to analyze such bumps together with the atomic location to figure out the transition barriers. Note that the local temperature provides the ergodicity for the atom to explore the minimum barrier path, while the external force provides the driving force for the atom to move along one direction. The potential curve will record the potential energy along the path, thus provide the potential barrier. If the external pulling force is very small, and if we can afford to wait for an extremely long time, then we will eventually see the correct barrier height from the potential energy along the path. A large pulling force might distort the results by forcing the atom to go through high barrier paths, but a moderate pulling force might at one hand reduce the transition time, and on the other hand, allow the atom to find the minimum energy path, thus not skew the result.

To test the robustness of our method, the Li migration barriers on a graphene surface are calculated by both NEB (b) and our model (a) as shown in Figure S4, supporting information. During the special Langevin MD with external force in our model, the lithium follows roughly the minimum energy path as we found from the NEB calculation. Thus the potential barrier calculated from our PA-MD is in excellent agreement with that of the NEB results. Note, the external force does not need to be in the same direction of the barrier path. If the force is not too big, the system will find the minimum barrier path. A good test of our method is to reduce the external force as long as the atom is still jumping within the simulation time, and find the barrier height no longer depends on the pulling force amplitude. In the above graphene case, the barrier we calculated from the NEB is 0.30 eV, while the barrier averaged from our PA-MD path is also about 0.30 eV. We do notice some fluctuation of the PA-MD potential path. Thus, there could be a 30% uncertainty in the obtained barrier height. Therefore, this method might not be extremely deterministic, nevertheless, it can provide critical information for a rough estimation of the barrier heights. For an amorphous system, this is exactly what we need.

For our Mn-HAB-Li_xS_y systems, a smaller external force, 0.5 eV/Å, and a larger external force 0.8 eV/Å in the X, and Z-direction, respectively, is applied on one Lithium atom of four systems at different lithiation stages. With PA-MD simulation for 5000 fs, the potential energy evolution with the lithium migration distance is shown in figure 4. Based on the migration distance, we classify the 16 charts into three categories: Force sufficient to drive the Li migration (migration distance larger than 20 Å, highlighted in green background color), Force insufficient to drive the Li migration (migration distance smaller than 5 Å, highlighted in gray background color), and the Intermediate state (migration distance larger than 5 Å but smaller than 20 Å, highlighted in yellow background color). A small force is enough to drive the lithium in the Li_5S_8-Mn-HAB moving in the X-direction. Meanwhile, the small force can also move the Lithium in the $Li_{10}S_8$-Mn-HAB and $Li_{15}S_8$-Mn-HAB in the Z-direction (for an atom in the hole of the stack) for a short distance (about 2-3 interlayer distances). With larger force in the X-direction, the lithium in the Li_5S_8-Mn-HAB, $Li_{10}S_8$-Mn-HAB, and $Li_{15}S_8$-Mn-HAB is movable for a long distance. However, the larger force in

the Z-direction can only drive the Lithium in the $Li_{10}S_8$-Mn-HAB and $Li_{15}S_8$-Mn-HAB to move. Therefore, in the early stage of lithiation (Li_5S_8-Mn-HAB), Li is difficult to move in the interlayer Z-direction but can move at the lateral direction between the Mn-HAB layers. At the intermediate lithiation stage ($Li_{10}S_8$-Mn-HAB and $Li_{15}S_8$-Mn-HAB), the Li is easier to move in the Z-direction (probably due to the connection of the Li-S between different layers in the hole of the stack), but more difficult to move along the lateral direction (probably due to too many Li-S between the Mn-HAB layers). At the end of the lithiation stage ($Li_{20}S_8$-Mn-HAB), it becomes difficult to move in any direction (probably because there are too many Li-S).
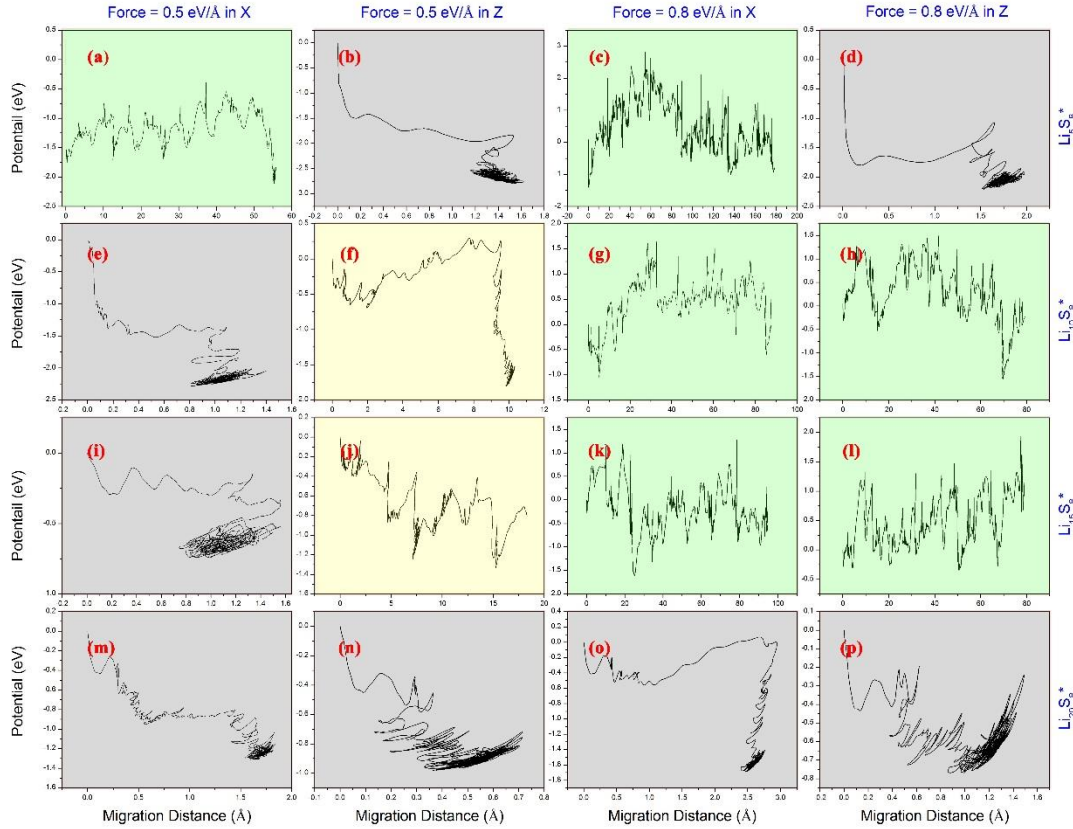

Figure 4 potential evolutions of Mn-HAB-Li_5S_8, Mn-HAB-$Li_{10}S_8$, Mn-HAB-$Li_{15}S_8$, and Mn-HAB-$Li_{20}S_8$ systems during the PA-MD simulations when an external force (0.5 eV/Å or 0.8 eV/Å in the X or Z-direction) applied on one Lithium. The X-direction is an in-layer direction, while the Z-direction is the interlayer direction. The different background colors represent Li migration status (green: Force sufficient to drive the Li migration; gray: force inefficient to drive the Li migration; and yellow: the intermediate state). Please note the different horizontal axis scale for the different colored panels. The migration distance is measured as the change of Li's coordinate in force direction.

To have a more quantitative estimation of the conductivity, we need to get the diffusion barrier. We will first ignore the sharp spikes within 1 Å in the potential plot in Fig.4. Such spikes might be caused by local oscillation or atom-atom collision instead of general transition barriers, in contrast, the barrier between local minimum should correspond to a distance in the range of 5 to 10 Å. To filter out such high oscillation, we use the following filter formula to smooth the curves in Fig. 4 (a), (c), (g), (h), (k) and (l).

$$E'(y) = \frac{\int_{y-3}^{y+3} E(x)e^{-(x-y)^4}dx}{\int_{y-3}^{y+3} e^{-(x-y)^4}dx} \qquad (8)$$

Here the x and y unit is in angstrom. The filtered curves are presented in Figure S5, supporting information. If both 0.5 eV/Å and 0.8 eV/Å pulling force can make a system move, we found that the larger force tends to give slightly higher barriers (in the range of 0.15 eV). In that case, we will use the barrier obtained from the smaller force results, as discussed above. But this barrier difference also gives us a sense of the upper bound of the uncertainty in this method, which is typically under 0.15 eV. It should mention that uncertainty related to the different initial conditions can be reduced in some extent by repeating the calculations. During the simulation (Mn-HAB-Li$_5$S$_8$ under external force of 0.5 eV/Å for example), the Li migrates about 55 Å in our amorphous system. We assume the Li atoms have explored different initial speed and position, and obtained many barrier values. The average barrier values are used to evaluate Li diffusion in these systems. On the other hand, due to the amorphous nature, there are indeed some uncertainty, depend on which atoms we choose. This uncertainty is also reduced in some extent by repeating the calculations for several atoms and take the averaged barrier. We do feel this method might have intrinsic fluctuations due to the amorphous nature of the system. The uncertainty of the barrier might be in the range of 0.1 eV. We thus us it as a rough estimation of the barrier heights. For an amorphous system, that is what we need. We also feel this method might slightly over estimated the barrier because we didn't consider any possible correlation effects for the diffusion between Li atoms. In a disorder amorphous system, it is possible that the Li atoms with the lowest barrier will diffuse first, and after this diffusion, it might provide new opportunity (vacancy site etc) for other Li to diffuse.
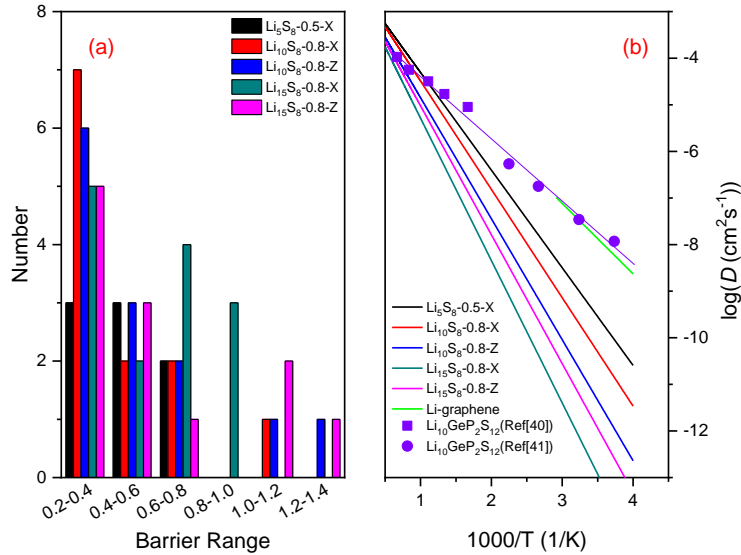

Figure 5 Li-migration barriers distribution (a) and diffusion coefficients as a function of temperature (b) of Mn-HAB-Li$_5$S$_8$, Mn-HAB-Li$_{10}$S$_8$, and Mn-HAB-Li$_{15}$S$_8$, in the X and Z-directions. The diffusion coefficients curves of Li on graphene and Li$_{10}$GeP$_2$S$_{12}$[30] are also presented as a reference.

Following the above procedure, we have obtained different barrier heights for different systems, and for different jumps within the same system. In reality, obtaining a distribution of different barrier heights in an amorphous system might be advantageous, since collectively, some Li will be able to find some lower barriers to diffuse, hence making the overall diffusion coefficient higher. Figure 5a plots the barrier distribution we obtained for different systems. The average migration barrier for Li_5S_8-0.5-X, $Li_{10}S_8$-0.8-X, $Li_{10}S_8$-0.8-X, $Li_{15}S_8$-0.8-X, and $Li_{15}S_8$-0.8-X is 0.42, 0.46, 0.52, 0.61 and 0.55 eV as list in Table S1, supporting information. It should be noted that these values are comparable with that of graphene (0.30 eV). Using these average barrier heights, and the Eq.(6), the Li diffusion coefficient in Mn-HAB-Li_5S_8, Mn-HAB-$Li_{10}S_8$, and Mn-HAB-$Li_{15}S_8$, in the X and Z-directions a function of temperature are calculated and presented in Figure 5b. We have to keep in mind that the diffusion coefficient shown in Fig.5b is estimated using the average barrier height. For comparison, the Li diffusion coefficient in graphene and $Li_{10}GeP_2S_{12}$[30] are exhibited as well. The diffusion coefficient for Li on LiC_6 ranges from 10^{-7} to 10^{-12} cm^2s^{-1}[31]. Due to the crowded Li in LiC_6, the diffusion coefficient of Li is expected to be smaller than that in perfect graphene. Our predicted diffusion coefficient of Li in graphene, 2.39×10^{-8} cm^2s^{-1}, is close to the upper limit of the experimental LiC_6 data and is in excellent agreement with the DFT calculated coefficient value on graphene in literature (3.70×10^{-8} cm^2s^{-1})[32]. The calculated diffusion coefficient of Li atom for Li_5S_8-0.5-X, $Li_{10}S_8$-0.8-X, $Li_{10}S_8$-0.8-Z, $Li_{15}S_8$-0.8-X, and $Li_{15}S_8$-0.8-Z at 300 K are 6.36×10^{-10} cm^2s^{-1}, 1.21×10^{-10} cm^2s^{-1}, 1.24×10^{-11} cm^2s^{-1}, 3.83×10^{-13} cm^2s^{-1}, and 3.33×10^{-12} cm^2s^{-1} respectively. It's worth noting that the Li_5S_8 has the highest Li diffusion coefficient, and it is about 1/38 of that in graphene (2.39×10^{-8} cm^2s^{-1}) and 1/52 of that in the excellent Li ionic conductor $Li_{10}GeP_2S_{12}$ ($\sim3.30\times 10^{-8}$)[30]. In addition, the Li diffusion coefficient of Li_5S_8-0.5-X, $Li_{10}S_8$-0.8-X, $Li_{10}S_8$-0.8-X, $Li_{15}S_8$-0.8-X, and $Li_{15}S_8$-0.8-X is better than or comparable with that of some well-known Li-ion battery cathode materials, like $LiFePO_4$[33], a-Li_3PO_4[34], $LiNi_{0.5}Mn_{1.5}O_4$[35]. The whole comparison is summarized in table S2 in supporting information. Overall, we believe the diffusion coefficient at low and intermediate lithiation stages should be adequate for the Li-S battery applications. However, the low Li diffusion coefficient at higher lithiation stage could be challenging for fast charging and discharging. One of the reasons is the overly packed system. One potential approach is to make the system less dense, thus provide more room for Li diffusion. Overall, we found that the breaking and formation of Li-S bond is not a problem for Li diffusion (as in the low and intermediate lithiation stage), but the overcrowded packing of Li-S can be a problem. This provides guidance for future compact Li-S cathode design.
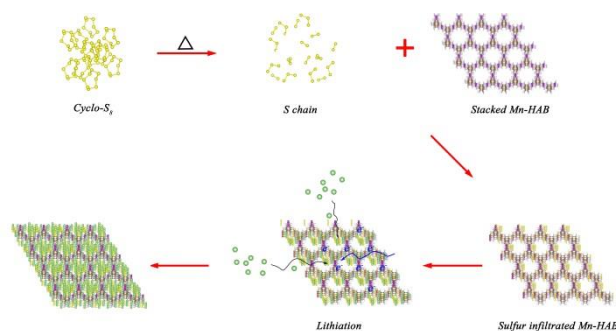

Figure 6 Schematic illustration of the preparation of Li-S cathode with Mn-HAB

Based on our theoretical investigation and experimental references[11, 15a, 36], it is interested to hypothesize the Li-S cathode preparation process with Mn-HAB as shown in figure 6. At high temperature (above 250 °C), cyclo-S_8 vapors and undergoes thermal scission into linear sulfur chains[37]. The Mn-HAB with particles sizes ranged from 1-50 *nm* can be synthesized via three simple steps: (1) metal coordination with the HAB ligand, (2) deprotonation of –NH_2 on HAB by the base and (3) oxidation of the deprotonated HAB. Then the Mn-HAB pellets with tunable thickness from 0.2 mm to 1.07 mm can be obtained via cold isostatic pressing. The linear sulfur chains are infiltrated into submillimeter-thick Mn-HAB through the holes[11]. The infiltrated sulfur chains tend to bind on the Mn-HAB via S-Mn bonds and exist as linear chains inside Mn-HAB. These Mn-HAB would have a good chemical stability in both acid and base aqueous environments, which allows for their use in low-cost and non-flammable aqueous electrolytes. Therefore, the common electrolytes (e.g., 1,2-dimethoxyethane(DME)/1,3-dioxolane(DOL) (1: 1, v: v)) and separator should work between the anode Li foil and the cathode designed here. As pointed out in our previous work(*Adv. Energy Mater.* **2018,** *8,* 1801823), one advantage of this material is the thermal-dynamic stability against Li_2S_n dissolution in the common electrolyte. We thus believe emerging this cathode in the organic electrolytes will work. During the lithiation process, the Li migrate into the Mn-HAB in the in-layer direction and the interlayer direction (through the holes), meanwhile the electron transfer through the metallic Mn-HAB from opposite direction.

Summary

In summary, we have proposed a Mn-HAB/Li-S sandwich structure as a prototype 3D Li-S cathode design. Such a compact 3D cathode design is to address the issue of volumetric capacity of Li-S cathode. The solid 3D design is an alternative to the commonly used designs of Li-S cathode where liquid electrolyte has to infiltrate into the cathode. Our theoretical investigation likes to answer the fundamental questions in such designs, including the limit of gravimetric and volumetric capacities, the structure stability, and most importantly the Li diffusion coefficient in such systems. We found that: (1) the pre-molten Sulfur increases the Mn-HAB/Mn-HAB interlayer distance, provides sufficient room for LiPSs during the lithiation process; (2) in the early stage of lithiation process, the coordination number of S is relatively low, the Mn-S is vital to suppressing the LiPS shuttle, while at the end stage, Li-N bonds play important role in stabilizing the LiPS; (3) the structure of the interlayer Li-S is amorphous; (4) upon full lithiation, the layer-layer distance can change 20%. While the distance increases initially, it shrinks upon full lithiation due to the movement of LiS towards the hole of the structure; (5) the cathode can have a theoretical gravimetric capacity of 825 Wh/Kg, and volumetric energy density of 1652 Wh/L; (6) the system is electrically conductive due to the Mn-HAB framework throughout the lithiation process; (7) the Li diffusion coefficient in the 3D Mn-HAB is better than or comparable with some well-known Li-ion battery cathode materials, like $LiFePO_4$[33], a-Li_3PO_4[34], $LiNi_{0.5}Mn_{1.5}O_4$[35], especially in the early and intermediate stages of lithiation. This means overall such compact solid Li-S cathode design can be practical. For the Li diffusion, the requirement of bond breaking and formation between Li and S might not be an issue, but overpacking of high Li density in Li-S might hinder the Li diffusion.

Finally, to study the structure of the amorphous system, we have used an in-house developed genetic algorithm to search the minimum energy atomic configuration. To study the Li diffusion in

the amorphous system where the conventional calculation method cannot be used, we have developed a special pull-atom MD approach. This approach yields the correct barrier heights for simple crystal structures, but also allows us to study complex amorphous systems. We believe this method can also be used to many other complex systems, especially for battery research.

Supporting information

The process of the in-house global minimum structure search code, the enlarge views of $Li_5S_8^*$ and $Li_{20}S_8^*$, the band structures of Mn-HAB, Mn-HAB-S_8, Mn-HAB-Li_5S_8, Mn-HAB-$Li_{10}S_8$, Mn-HAB-$Li_{15}S_8$, and Mn-HAB-$Li_{20}S_8$, the barrier of Li migration on the graphene, the fitted potential evolutions of Li migration in Mn-HAB-Li_5S_8, Mn-HAB-$Li_{10}S_8$, and Mn-HAB-$Li_{15}S_8$, key parameters for Li diffusion, comparison of Li-ion diffusion coefficient from the present work with available literature data in Li-ion battery can be found in the supporting information.

Acknowledgment

Reference

1. Seh, Z. W.; Sun, Y.; Zhang, Q.; Cui, Y., Designing high-energy lithium–sulfur batteries. *Chem. Soc. Rev.* **2016,** *45* (20), 5605-5634.

2. Peng, H.-J.; Huang, J.-Q.; Cheng, X.-B.; Zhang, Q., Review on High-Loading and High-Energy Lithium–Sulfur Batteries. *Adv. Energy Mater.* **2017,** *7* (24), 1700260.

3. Sun, Z.; Zhang, J.; Yin, L.; Hu, G.; Fang, R.; Cheng, H.-M.; Li, F., Conductive porous vanadium nitride/graphene composite as chemical anchor of polysulfides for lithium-sulfur batteries. *Nat. Commun.* **2017,** *8*, 14627.

4. Pang, Q.; Liang, X.; Kwok, C. Y.; Nazar, L. F., Advances in lithium–sulfur batteries based on multifunctional cathodes and electrolytes. *Nat. Energy* **2016,** *1*, 16132.

5. Bruce, P. G.; Freunberger, S. A.; Hardwick, L. J.; Tarascon, J.-M., Li–O_2 and Li–S batteries with high energy storage. *Nat. Mater.* **2011,** *11*, 19-29.

6. Ji, X.; Lee, K. T.; Nazar, L. F., A highly ordered nanostructured carbon–sulphur cathode for lithium–sulphur batteries. *Nat. Mater.* **2009,** *8*, 500-506.

7. Jayaprakash, N.; Shen, J.; Moganty, S. S.; Corona, A.; Archer, L. A., Porous Hollow Carbon@Sulfur Composites for High-Power Lithium–Sulfur Batteries. *Angew. Chem.* **2011,** *50* (26), 5904-5908.

8. He, G.; Evers, S.; Liang, X.; Cuisinier, M.; Garsuch, A.; Nazar, L. F., Tailoring Porosity in Carbon Nanospheres for Lithium–Sulfur Battery Cathodes. *ACS Nano* **2013,** *7* (12), 10920-10930.

9. Zhou, G.; Yin, L.-C.; Wang, D.-W.; Li, L.; Pei, S.; Gentle, I. R.; Li, F.; Cheng, H.-M., Fibrous Hybrid of Graphene and Sulfur Nanocrystals for High-Performance Lithium–Sulfur Batteries. *ACS Nano* **2013,** *7* (6), 5367-5375.

10. Ji, L.; Rao, M.; Zheng, H.; Zhang, L.; Li, Y.; Duan, W.; Guo, J.; Cairns, E. J.; Zhang, Y., Graphene Oxide as a Sulfur Immobilizer in High Performance Lithium/Sulfur Cells. *J. Am. Chem. Soc.* **2011,** *133* (46), 18522-18525.

11. Wu, J.; Wang, L.-W., 2D framework C_2N as a potential cathode for lithium-sulfur batteries: an *ab initio* density functional study. *J. Mater. Chem. A* **2018,** *6* (7), 2984-2994.

12. Wang, Z.; Dong, Y.; Li, H.; Zhao, Z.; Bin Wu, H.; Hao, C.; Liu, S.; Qiu, J.; Lou, X. W., Enhancing lithium–sulphur battery performance by strongly binding the discharge products on amino-functionalized reduced graphene oxide. *Nat. Commun.* **2014,** *5*, 5002.

13. Zhao, Z.; Wang, S.; Liang, R.; Li, Z.; Shi, Z.; Chen, G., Graphene-wrapped chromium-MOF(MIL-101)/sulfur composite for performance improvement of high-rate rechargeable Li–S batteries. *J. Mater. Chem. A* **2014,** *2* (33), 13509-13512.

14. Guan, C.; Liu, X.; Ren, W.; Li, X.; Cheng, C.; Wang, J., Rational Design of Metal-Organic Framework Derived Hollow $NiCo_2O_4$ Arrays for Flexible Supercapacitor and Electrocatalysis. *Adv. Energy Mater.* **2017,** *7* (12), 1602391.

15. Lahiri, N.; Lotfizadeh, N.; Tsuchikawa, R.; Deshpande, V. V.; Louie, J., Hexaaminobenzene as a building block for a Family of 2D Coordination Polymers. *J. Am. Chem. Soc.* **2017,** *139* (1), 19-22.

16. Feng, D.; Lei, T.; Lukatskaya, M. R.; Park, J.; Huang, Z.; Lee, M.; Shaw, L.; Chen, S.; Yakovenko, A. A.; Kulkarni, A.; Xiao, J.; Fredrickson, K.; Tok, J. B.; Zou, X.; Cui, Y.; Bao, Z., Robust and conductive two-dimensional metal−organic frameworks with exceptionally high volumetric and areal capacitance. *Nat. Energy* **2018,** *3* (1), 30-36.

17. Gao, G.; Zheng, F.; Pan, F.; Wang, L.-W., Theoretical Investigation of 2D Conductive Microporous Coordination Polymers as Li–S Battery Cathode with Ultrahigh Energy Density. *Adv. Energy Mater.* **2018,** *8* (25), 1801823.

18. OXIS-Energy-Ltd, Our Cell and Battery Technology Advantages. https://oxisenergy.com/technology/, 2019.

19. Liu, Y.; Zhou, G.; Liu, K.; Cui, Y., Design of Complex Nanomaterials for Energy Storage: Past Success and Future Opportunity. *Acc. Chem. Res.* **2017,** *50* (12), 2895-2905.

20. Xue, W.; Miao, L.; Qie, L.; Wang, C.; Li, S.; Wang, J.; Li, J., Gravimetric and volumetric energy densities of lithium-sulfur batteries. *Curr. Opin. Electrochem.* **2017,** *6* (1), 92-99.

21. Pope, M. A.; Aksay, I. A., Structural Design of Cathodes for Li-S Batteries. *Adv. Energy Mater.* **2015,** *5* (16), 1500124.

22. Helen, M.; Diemant, T.; Schindler, S.; Behm, R. J.; Danzer, M.; Kaiser, U.; Fichtner, M.; Anji Reddy, M., Insight into Sulfur Confined in Ultramicroporous Carbon. *ACS Omega* **2018,** *3* (9), 11290-11299.

23. Yin, Y.; Franco, A. A., Unraveling the Operation Mechanisms of Lithium Sulfur Batteries with Ultramicroporous Carbons. *ACS Appl. Energy Mater.* **2018,** *1* (11), 5816-5821.

24. Liu, D.; Zhu, W.; Feng, Z.; Guerfi, A.; Vijh, A.; Zaghib, K., Recent progress in sulfide-based solid electrolytes for Li-ion batteries. *Mater. Sci. Eng. B* **2016,** *213*, 169-176.

25. Miara, L. J.; Ong, S. P.; Mo, Y.; Richards, W. D.; Park, Y.; Lee, J.-M.; Lee, H. S.; Ceder, G., Effect of Rb and Ta Doping on the Ionic Conductivity and Stability of the Garnet $Li_{7+2x-y}(La_{3-x}Rb_x)(Zr_{2-y}Ta_y)O12$ ($0 \leqslant x \leqslant 0.375$, $0 \leqslant y \leqslant 1$) Superionic Conductor: A First Principles Investigation. *Chem. Mater.* **2013,** *25* (15), 3048-3055.

26. Yu, S.; Rao, Y.-C.; Li, S.-F.; Duan, X.-M., Net W monolayer: A high-performance electrode material for Li-ion batteries. *Appl. Phys. Lett.* **2018,** *112* (5), 053903.

27. Voter, A. F. In *Introduction to the Kinetic Monte Carlo Method*, Dordrecht, Springer Netherlands: Dordrecht, 2007; pp 1-23.

28. Laio, A.; Parrinello, M., Escaping free-energy minima. *Proc. Natl. Acad. Sci.* **2002,** *99* (20), 12562-6.

29.   Hiebl, C.; Young, D.; Wagner, R.; Wilkening, H. M. R.; Redhammer, G. J.; Rettenwander, D., Proton Bulk Diffusion in Cubic $Li_7La_3Zr_2O_{12}$ Garnets as Probed by Single X-ray Diffraction. *J. Phys. Chem. C* **2019,** *123* (2), 1094-1098.

30.   Jia, W.; Cao, Z.; Wang, L.; Fu, J.; Chi, X.; Gao, W.; Wang, L.-W., The analysis of a plane wave pseudopotential density functional theory code on a GPU machine. *Comput. Phys. Commun.* **2013,** *184* (1), 9-18.

31.   Jia, W.; Fu, J.; Cao, Z.; Wang, L.; Chi, X.; Gao, W.; Wang, L.-W., Fast plane wave density functional theory molecular dynamics calculations on multi-GPU machines. *J. Comput. Phys.* **2013,** *251* (Supplement C), 102-115.

32.   Perdew, J. P.; Burke, K.; Ernzerhof, M., Generalized Gradient Approximation Made Simple. *Phys. Rev. Lett.* **1996,** *77* (18), 3865-3868.

33.   Perdew, J. P.; Ernzerhof, M.; Burke, K., Rationale for mixing exact exchange with density functional approximations. *J. Chem. Phys.* **1996,** *105* (22), 9982-9985.

34.   Grimme, S., Semiempirical GGA-type density functional constructed with a long-range dispersion correction. *J. Comput. Chem.* **2006,** *27* (15), 1787-1799.

35.   Dudarev, S. L.; Botton, G. A.; Savrasov, S. Y.; Humphreys, C. J.; Sutton, A. P., Electron-energy-loss spectra and the structural stability of nickel oxide: An LSDA+U study. *Phys. Rev. B* **1998,** *57* (3), 1505-1509.

36.   Darby, S.; Mortimer-Jones, T. V.; Johnston, R. L.; Roberts, C., Theoretical study of Cu–Au nanoalloy clusters using a genetic algorithm. *J. Chem. Phys.* **2002,** *116* (4), 1536-1550.

37.   von Smoluchowski, M., Zur kinetischen Theorie der Brownschen Molekularbewegung und der Suspensionen. *Ann. Phys.* **1906,** *326* (14), 756-780.

38.   Chandrasekhar, S., Stochastic Problems in Physics and Astronomy. *Rev. Mod. Phys.* **1943,** *15* (1), 1-89.

39.   Klein, M. J.; Veith, G. M.; Manthiram, A., Chemistry of Sputter-Deposited Lithium Sulfide Films. *J. Am. Chem. Soc.* **2017,** *139* (31), 10669-10676.

40.   Mo, Y.; Ong, S. P.; Ceder, G., First Principles Study of the $Li_{10}GeP_2S_{12}$ Lithium Super Ionic Conductor Material. *Chem. Mater.* **2012,** *24* (1), 15-17.

41.   Kuhn, A.; Duppel, V.; Lotsch, B. V., Tetragonal $Li_{10}GeP_2S_{12}$ and Li_7GePS_8 – exploring the Li ion dynamics in LGPS Li electrolytes. *Energy Environ. Sci.* **2013,** *6* (12), 3548-3552.

42.   Zempachi, O.; Minoru, I., Electrochemical Lithium Intercalation within Carbonaceous Materials: Intercalation Processes, Surface Film Formation, and Lithium Diffusion. *Bull. Chem. Soc. Jpn.* **1998,** *71* (3), 521-534.

43.   NuLi, Y.; Yang, J.; Jiang, Z., Intercalation of lithium ions into bulk and powder highly oriented pyrolytic graphite. *J. Phys. Chem. Solids* **2006,** *67* (4), 882-886.

44.   Kubota, Y.; Ozawa, N.; Nakanishi, H.; Kasai, H., Quantum States and Diffusion of Lithium Atom Motion on a Graphene. *J. Phys. Soc. Jpn.* **2009,** *79* (1), 014601.

45.   Prosini, P. P.; Lisi, M.; Zane, D.; Pasquali, M., Determination of the chemical diffusion coefficient of lithium in $LiFePO_4$. *Solid State Ion.* **2002,** *148* (1), 45-51.

46.   Kuwata, N.; Lu, X.; Miyazaki, T.; Iwai, Y.; Tanabe, T.; Kawamura, J., Lithium diffusion coefficient in amorphous lithium phosphate thin films measured by secondary ion mass spectroscopy with isotope exchange methods. *Solid State Ion.* **2016,** *294*, 59-66.

47.   Liu, W.; Shi, Q.; Qu, Q.; Gao, T.; Zhu, G.; Shao, J.; Zheng, H., Improved Li-ion diffusion and stability of a $LiNi_{0.5}Mn_{1.5}O_4$ cathode through in situ co-doping with dual-metal cations and incorporation of a

superionic conductor. *J. Mater. Chem. A* **2017,** *5* (1), 145-154.

48.   Fang, R.; Zhao, S.; Wang, D.-W.; Sun, Z.; Cheng, H.-M.; Li, F., Micro-Macroscopic Coupled Electrode Architecture for High-Energy-Density Lithium–Sulfur Batteries. *ACS Appl. Energy Mater.* **2019,** *2* (10), 7393-7402.

49.   Hong, X.-J.; Tang, X.-Y.; Wei, Q.; Song, C.-L.; Wang, S.-Y.; Dong, R.-F.; Cai, Y.-P.; Si, L.-P., Efficient Encapsulation of Small S_{2-4} Molecules in MOF-Derived Flowerlike Nitrogen-Doped Microporous Carbon Nanosheets for High-Performance Li–S Batteries. *ACS Appl. Mater. Interfaces* **2018,** *10* (11), 9435-9443.

50.   Meyer, B., Elemental sulfur. *Chem. Rev.* **1976,** *76* (3), 367-388.
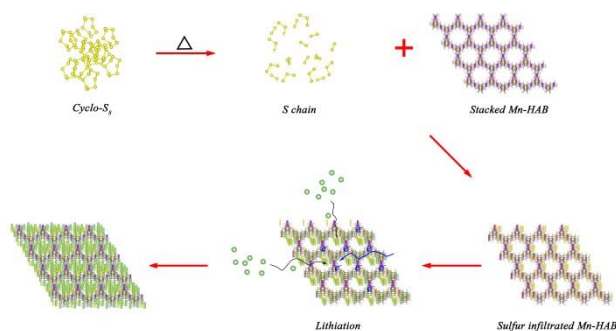
Supplementary Information

A solid 3D Li-S battery design via stacking 2D conductive microporous coordination polymers and amorphous Li-S layers

Guoping Gao, Fan Zheng, Lin-Wang Wang*

Materials Sciences Division, Lawrence Berkeley National Laboratory, Berkeley, California 94720, USA. E-mail: lwwang@lbl.gov

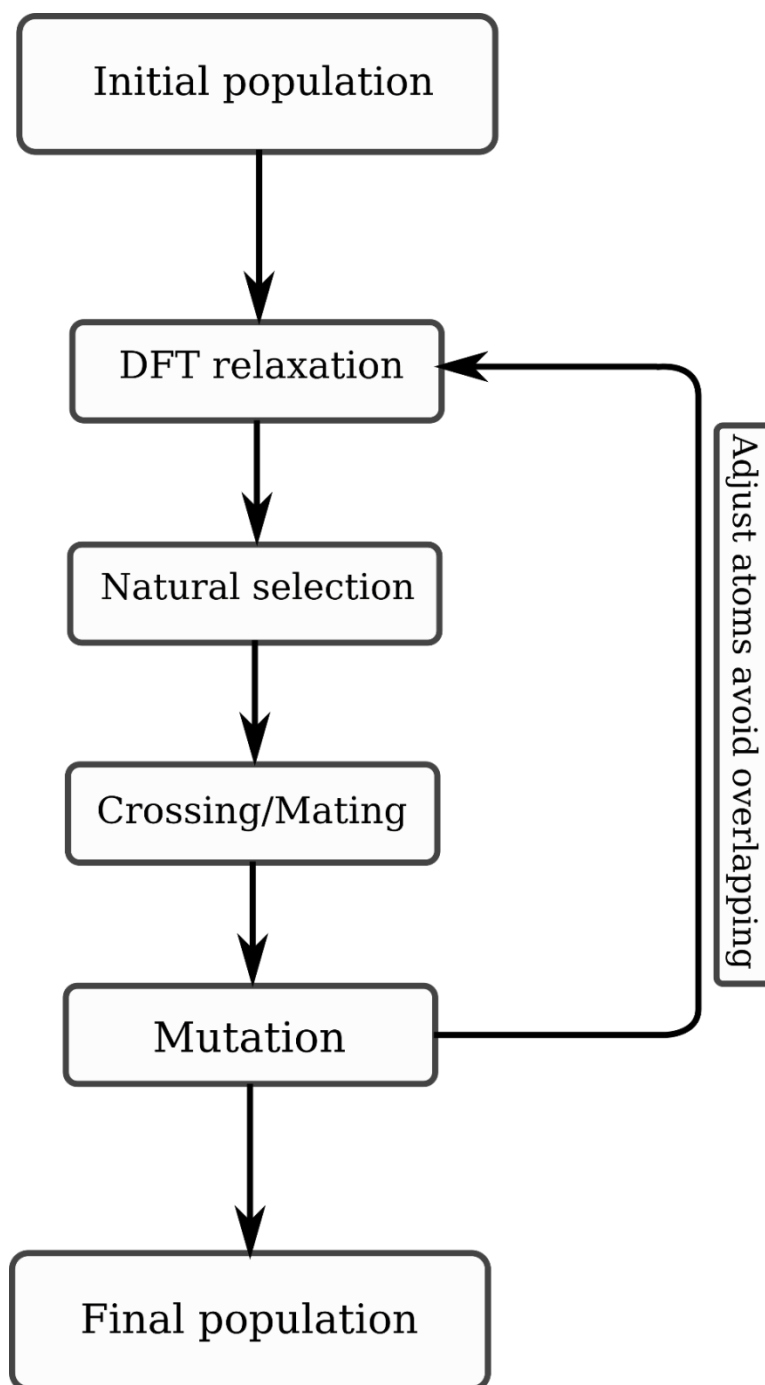1. **The process of the in-house global minimum structure search code**

Figure S7 The process of the in-house global minimum structure search code.

In this optimization scheme, each generation contains 10 structures. One major feature is to generate new structures of the absorbed molecule/cluster, while keep the structure of the substrate unchanged (although it will be moved during relaxation). The initial generation for each structure is obtained with random atomic Li and S positions on fixed 3D Mn-HAB. DFT relaxations for all the 10 structures are

performed, and the energies of the relaxed structure are sorted from lowest to highest. By natural selection, we pick up two structures out of the whole population to form a pair for crossing. The probability of picking structure i is controlled by the fitness factor as $\exp(-\lambda*(E_i-E_{min})/(E_{max}-E_{min}))$. The λ is set to 2 obtained from Ref[27]. For the crossing process of the two structures, we randomly choose Li or S atoms from each structure and rotate the whole structure along z-axis so that the picked atoms are along the x-direction for both structures. The crossing is processed by coding all the Li and S atoms of a structure into a 1-d array using the x-component of the atomic coordinates. The number of Li and S atoms are re-counting so that they are conserved for each crossing/mating trial. By random selecting a point along with the two 1-d arrays, these two arrays are crossovered so that we can obtain a mated structure out of the two structures. A pre-relaxation is performed via a steep-descent method to avoid too-close atoms. Then DFT relaxations are used to relax all the child structures and obtain their energies. We then repeat the natural selection as mentioned above. As energies of the lowest structure do not change after many generations, we believe the global minimum structure is obtained.

2. **The enlarged views of Li_5S_8* and $Li_{20}S_8*$.**
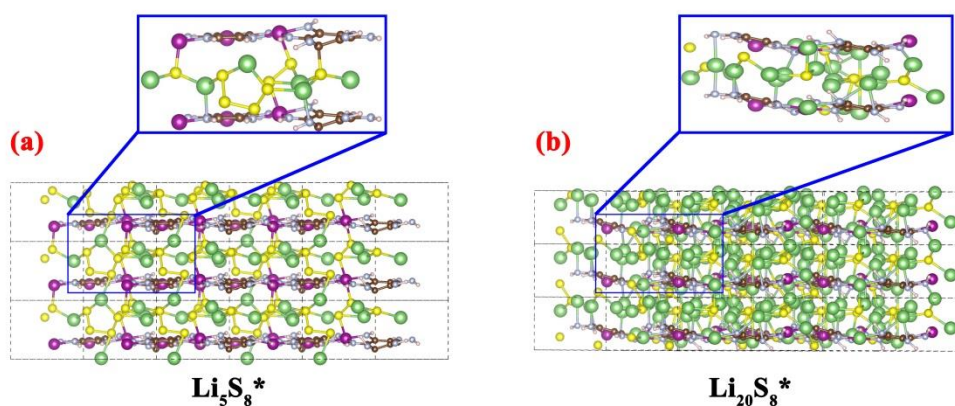

Figure S8 the enlarged views of Li_5S_8* and $Li_{20}S_8*$. The bond length cut-off for Mn-S is 2.4 Å, for N-Li is 2.4 Å, for S-S is 2.4Å, for Li-S is 2.6 Å, and for possible Mn-Li is 2.6 Å.

3. **The Band structures of Mn-HAB, Mn-HAB-S$_8$, Mn-HAB-Li$_5$S$_8$, Mn-HAB-Li$_{10}$S$_8$, Mn-HAB-Li$_{15}$S$_8$, and Mn-HAB-Li$_{20}$S$_8$.**
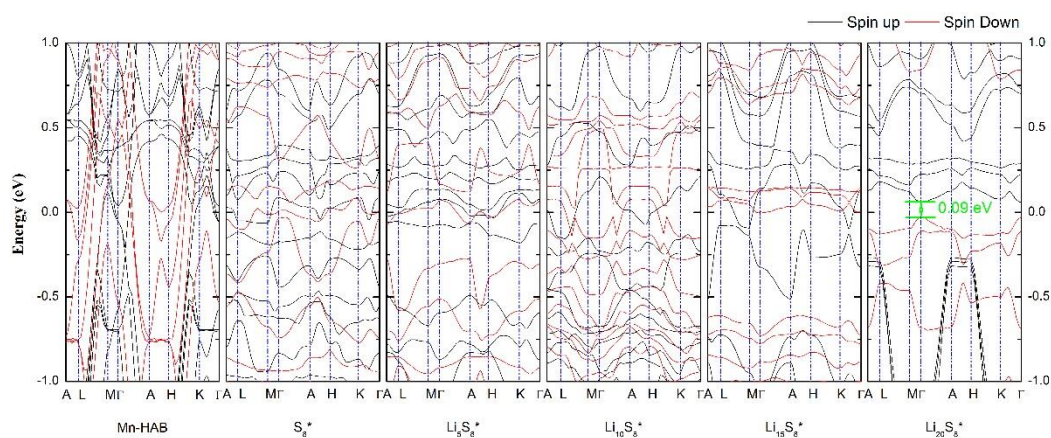
Figure S9. Band structures of Mn-HAB, Mn-HAB-S$_8$, Mn-HAB-Li$_5$S$_8$, Mn-HAB-Li$_{10}$S$_8$, Mn-HAB-Li$_{15}$S$_8$, and Mn-HAB-Li$_{20}$S$_8$. The Femi level is set to zero.

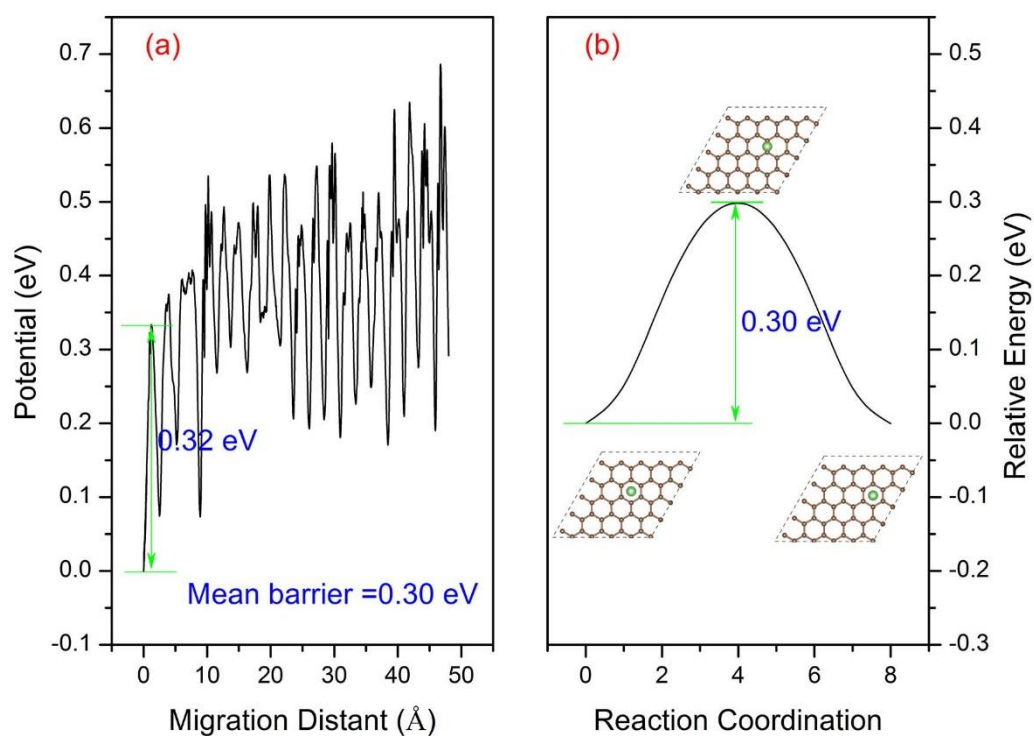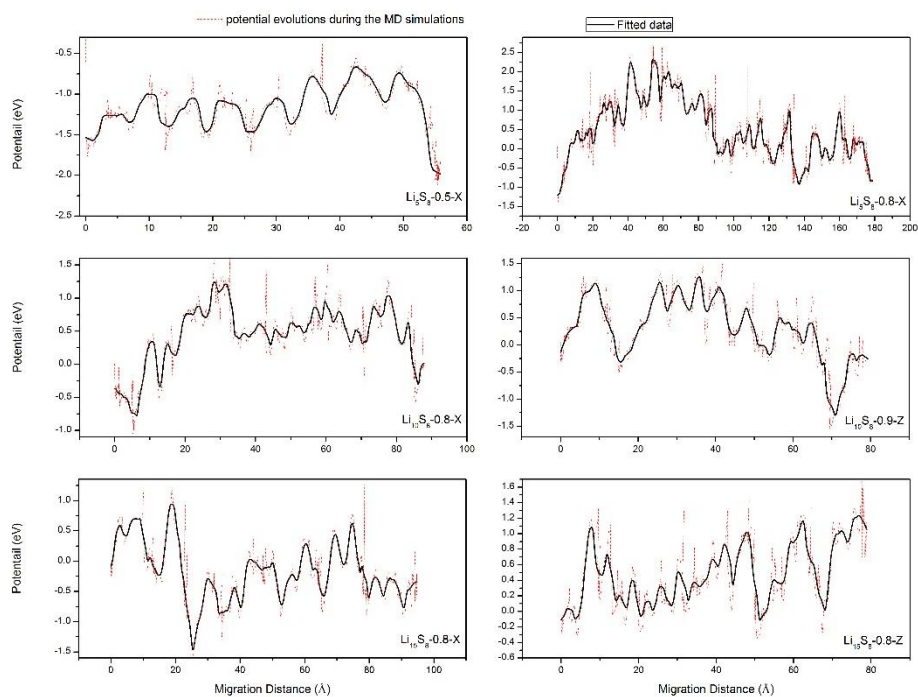4. **The barrier of Li migration on the graphene**

Figure S10 The barrier of Li migration on the graphene obtained by our model (a) and NEB calculation (b).

5. **The fitted potential evolutions of Li migration in Mn-HAB-Li5S8, Mn-HAB-Li10S8, and Mn-HAB-Li15S8.**

6. **Key parameters for Li diffusion**

Table S1 The average barriers and diffusion rate of Li migration in Mn-HAB-Li$_5$S$_8$, Mn-HAB-Li$_{10}$S$_8$, and Mn-HAB-Li$_{15}$S$_8$.

	Li$_5$S$_8$-0.5-X	Li$_{10}$S$_8$-0.8-X	Li$_{10}$S$_8$-0.8-Z	Li$_{15}$S$_8$-0.8-X	Li$_{15}$S$_8$-0.8-Z	graphene
Average barrier (eV)	0.42	0.46	0.52	0.61	0.55	0.30
d (Å)	6.93	7.31	6.61	6.76	6.57	3.28

7. Comparison of lithium ion diffusion coefficient from the present work with available literature data in Li-ion battery.

Table S2 The diffusion coefficient of different cathode and electrolyte

Composition	Diffusion coefficient (cm²s⁻¹)	Reference
Li_5S_8-0.5-X	6.36×10^{-10}	This study
$Li_{10}S_8$-0.8-X	1.21×10^{-10}	This study
$Li_{10}S_8$-0.8-Z	1.24×10^{-11}	This study
$Li_{15}S_8$-0.8-X	3.83×10^{-13}	This study
$Li_{15}S_8$-0.8-Z	3.33×10^{-12}	This study
graphene	2.39×10^{-8}	This study
$LiNi_{0.50}Mn_{0.20}Co_{0.30}O_2$ (NMC$_{523}$)	4.5×10^{-8}	38
$LiNi_{0.33}Mn_{0.33}Co_{0.33}O_2$ (NMC$_{333}$)	5.5×10^{-8}	38
$LiFePO_4$	1.8×10^{-14}	33
LNMO/LLZO (50 : 1)	1.83×10^{-10}	35
$LiNi_{0.5}Mn_{1.5}O_4$	6.43×10^{-11}	35
a-Li_3PO_4	6.0×10^{-13}	34
Cubic LLZO:Al	$\sim 10^{-9}$	22
$LiTi_2(PS_4)_3$	1.2×10^{-7}	39
$Li_{10}GeP_2S_{12}$	$\sim 3.30 \times 10^{-8}$	30

Reference

1.   (a) Seh, Z. W.; Sun, Y.; Zhang, Q.; Cui, Y., Designing high-energy lithium–sulfur batteries. *Chem. Soc. Rev.* **2016,** *45* (20), 5605-5634; (b) Peng, H.-J.; Huang, J.-Q.; Cheng, X.-B.; Zhang, Q., Review on High-Loading and High-Energy Lithium–Sulfur Batteries. *Adv. Energy Mater.* **2017,** *7* (24), 1700260.

2.   Sun, Z.; Zhang, J.; Yin, L.; Hu, G.; Fang, R.; Cheng, H.-M.; Li, F., Conductive porous vanadium nitride/graphene composite as chemical anchor of polysulfides for lithium-sulfur batteries. *Nat. Commun.* **2017,** *8*, 14627.

3.   Pang, Q.; Liang, X.; Kwok, C. Y.; Nazar, L. F., Advances in lithium–sulfur batteries based on multifunctional cathodes and electrolytes. *Nat. Energy* **2016,** *1*, 16132.

4.   Bruce, P. G.; Freunberger, S. A.; Hardwick, L. J.; Tarascon, J.-M., Li–O₂ and Li–S batteries with high energy storage. *Nat. Mater.* **2011,** *11*, 19-29.

5.   (a) Ji, X.; Lee, K. T.; Nazar, L. F., A highly ordered nanostructured carbon–sulphur cathode for lithium–sulphur batteries. *Nat. Mater.* **2009,** *8*, 500-506; (b) Jayaprakash, N.; Shen, J.; Moganty, S. S.; Corona, A.; Archer, L. A., Porous Hollow Carbon@Sulfur Composites for High-Power Lithium–Sulfur Batteries. *Angew. Chem.* **2011,** *50* (26), 5904-5908; (c) He, G.; Evers, S.; Liang, X.; Cuisinier, M.; Garsuch, A.; Nazar, L. F., Tailoring Porosity in Carbon Nanospheres for Lithium–Sulfur Battery Cathodes. *ACS Nano* **2013,** *7* (12), 10920-10930.

6.   (a) Zhou, G.; Yin, L.-C.; Wang, D.-W.; Li, L.; Pei, S.; Gentle, I. R.; Li, F.; Cheng, H.-M., Fibrous Hybrid of Graphene and Sulfur Nanocrystals for High-Performance Lithium–Sulfur Batteries. *ACS Nano* **2013,** *7* (6), 5367-5375; (b) Ji, L.; Rao, M.; Zheng, H.; Zhang, L.; Li, Y.; Duan, W.; Guo, J.; Cairns, E. J.; Zhang, Y., Graphene Oxide as a Sulfur Immobilizer in High Performance Lithium/Sulfur Cells. *J. Am. Chem. Soc.*

2011, *133* (46), 18522-18525.

7.   Wu, J.; Wang, L.-W., 2D framework C_2N as a potential cathode for lithium-sulfur batteries: an *ab initio* density functional study. *J. Mater. Chem. A* **2018,** *6* (7), 2984-2994.

8.   Wang, Z.; Dong, Y.; Li, H.; Zhao, Z.; Bin Wu, H.; Hao, C.; Liu, S.; Qiu, J.; Lou, X. W., Enhancing lithium–sulphur battery performance by strongly binding the discharge products on amino-functionalized reduced graphene oxide. *Nat. Commun.* **2014,** *5*, 5002.

9.   (a) Zhao, Z.; Wang, S.; Liang, R.; Li, Z.; Shi, Z.; Chen, G., Graphene-wrapped chromium-MOF(MIL-101)/sulfur composite for performance improvement of high-rate rechargeable Li–S batteries. *J. Mater. Chem. A* **2014,** *2* (33), 13509-13512; (b) Guan, C.; Liu, X.; Ren, W.; Li, X.; Cheng, C.; Wang, J., Rational Design of Metal-Organic Framework Derived Hollow $NiCo_2O_4$ Arrays for Flexible Supercapacitor and Electrocatalysis. *Adv. Energy Mater.* **2017,** *7* (12), 1602391.

10.   Lahiri, N.; Lotfizadeh, N.; Tsuchikawa, R.; Deshpande, V. V.; Louie, J., Hexaaminobenzene as a building block for a Family of 2D Coordination Polymers. *J. Am. Chem. Soc.* **2017,** *139* (1), 19-22.

11.   Feng, D.; Lei, T.; Lukatskaya, M. R.; Park, J.; Huang, Z.; Lee, M.; Shaw, L.; Chen, S.; Yakovenko, A. A.; Kulkarni, A.; Xiao, J.; Fredrickson, K.; Tok, J. B.; Zou, X.; Cui, Y.; Bao, Z., Robust and conductive two-dimensional metal−organic frameworks with exceptionally high volumetric and areal capacitance. *Nat. Energy* **2018,** *3* (1), 30-36.

12.   (a) OXIS-Energy-Ltd, Our Cell and Battery Technology Advantages. https://oxisenergy.com/technology/, 2019; (b) Liu, Y.; Zhou, G.; Liu, K.; Cui, Y., Design of Complex Nanomaterials for Energy Storage: Past Success and Future Opportunity. *Acc. Chem. Res.* **2017,** *50* (12), 2895-2905.

13.   Xue, W.; Miao, L.; Qie, L.; Wang, C.; Li, S.; Wang, J.; Li, J., Gravimetric and volumetric energy densities of lithium-sulfur batteries. *Curr. Opin. Electrochem.* **2017,** *6* (1), 92-99.

14.   Pope, M. A.; Aksay, I. A., Structural Design of Cathodes for Li-S Batteries. *Adv. Energy Mater.* **2015,** *5* (16), 1500124.

15.   (a) Helen, M.; Diemant, T.; Schindler, S.; Behm, R. J.; Danzer, M.; Kaiser, U.; Fichtner, M.; Anji Reddy, M., Insight into Sulfur Confined in Ultramicroporous Carbon. *ACS Omega* **2018,** *3* (9), 11290-11299; (b) Yin, Y.; Franco, A. A., Unraveling the Operation Mechanisms of Lithium Sulfur Batteries with Ultramicroporous Carbons. *ACS Appl. Energy Mater.* **2018,** *1* (11), 5816-5821.

16.   Liu, D.; Zhu, W.; Feng, Z.; Guerfi, A.; Vijh, A.; Zaghib, K., Recent progress in sulfide-based solid electrolytes for Li-ion batteries. *Mater. Sci. Eng. B* **2016,** *213*, 169-176.

17.   Gao, G.; Zheng, F.; Pan, F.; Wang, L.-W., Theoretical Investigation of 2D Conductive Microporous Coordination Polymers as Li–S Battery Cathode with Ultrahigh Energy Density. *Adv. Energy Mater.* **2018,** *8* (25), 1801823.

18.   Miara, L. J.; Ong, S. P.; Mo, Y.; Richards, W. D.; Park, Y.; Lee, J.-M.; Lee, H. S.; Ceder, G., Effect of Rb and Ta Doping on the Ionic Conductivity and Stability of the Garnet $Li_{7+2x-y}(La_{3-x}Rb_x)(Zr_{2-y}Ta_y)O12$ ($0 \leqslant x \leqslant 0.375, 0 \leqslant y \leqslant 1$) Superionic Conductor: A First Principles Investigation. *Chem. Mater.* **2013,** *25* (15), 3048-3055.

19.   Yu, S.; Rao, Y.-C.; Li, S.-F.; Duan, X.-M., Net W monolayer: A high-performance electrode material for Li-ion batteries. *Appl. Phys. Lett.* **2018,** *112* (5), 053903.

20.   Voter, A. F. In *Introduction to the Kinetic Monte Carlo Method*, Dordrecht, Springer Netherlands: Dordrecht, 2007; pp 1-23.

21.   Laio, A.; Parrinello, M., Escaping free-energy minima. *Proc. Natl. Acad. Sci.* **2002,** *99* (20), 12562-6.

22.   Hiebl, C.; Young, D.; Wagner, R.; Wilkening, H. M. R.; Redhammer, G. J.; Rettenwander, D., Proton Bulk Diffusion in Cubic $Li_7La_3Zr_2O_{12}$ Garnets as Probed by Single X-ray Diffraction. *J. Phys. Chem. C* **2019,** *123* (2), 1094-1098.

23.   (a) Jia, W.; Cao, Z.; Wang, L.; Fu, J.; Chi, X.; Gao, W.; Wang, L.-W., The analysis of a plane wave pseudopotential density functional theory code on a GPU machine. *Comput. Phys. Commun.* **2013,** *184* (1), 9-18; (b) Jia, W.; Fu, J.; Cao, Z.; Wang, L.; Chi, X.; Gao, W.; Wang, L.-W., Fast plane wave density functional theory molecular dynamics calculations on multi-GPU machines. *J. Comput. Phys.* **2013,** *251* (Supplement C), 102-115.

24.   (a) Perdew, J. P.; Burke, K.; Ernzerhof, M., Generalized Gradient Approximation Made Simple. *Phys. Rev. Lett.* **1996,** *77* (18), 3865-3868; (b) Perdew, J. P.; Ernzerhof, M.; Burke, K., Rationale for mixing exact exchange with density functional approximations. *J. Chem. Phys.* **1996,** *105* (22), 9982-9985.

25.   Grimme, S., Semiempirical GGA-type density functional constructed with a long-range dispersion correction. *J. Comput. Chem.* **2006,** *27* (15), 1787-1799.

26.   Dudarev, S. L.; Botton, G. A.; Savrasov, S. Y.; Humphreys, C. J.; Sutton, A. P., Electron-energy-loss spectra and the structural stability of nickel oxide: An LSDA+U study. *Phys. Rev. B* **1998,** *57* (3), 1505-1509.

27. Darby, S.; Mortimer-Jones, T. V.; Johnston, R. L.; Roberts, C., Theoretical study of Cu–Au nanoalloy clusters using a genetic algorithm. *J. Chem. Phys.* **2002,** *116* (4), 1536-1550.

28.   (a) von Smoluchowski, M., Zur kinetischen Theorie der Brownschen Molekularbewegung und der Suspensionen. *Ann. Phys.* **1906,** *326* (14), 756-780; (b) Chandrasekhar, S., Stochastic Problems in Physics and Astronomy. *Rev. Mod. Phys.* **1943,** *15* (1), 1-89.

29.   Klein, M. J.; Veith, G. M.; Manthiram, A., Chemistry of Sputter-Deposited Lithium Sulfide Films. *J. Am. Chem. Soc.* **2017,** *139* (31), 10669-10676.

30.   (a) Mo, Y.; Ong, S. P.; Ceder, G., First Principles Study of the $Li_{10}GeP_2S_{12}$ Lithium Super Ionic Conductor Material. *Chem. Mater.* **2012,** *24* (1), 15-17; (b) Kuhn, A.; Duppel, V.; Lotsch, B. V., Tetragonal $Li_{10}GeP_2S_{12}$ and Li_7GePS_8 – exploring the Li ion dynamics in LGPS Li electrolytes. *Energy Environ. Sci.* **2013,** *6* (12), 3548-3552.

31.   (a) Zempachi, O.; Minoru, I., Electrochemical Lithium Intercalation within Carbonaceous Materials: Intercalation Processes, Surface Film Formation, and Lithium Diffusion. *Bull. Chem. Soc. Jpn.* **1998,** *71* (3), 521-534; (b) NuLi, Y.; Yang, J.; Jiang, Z., Intercalation of lithium ions into bulk and powder highly oriented pyrolytic graphite. *J. Phys. Chem. Solids* **2006,** *67* (4), 882-886.

32.   Kubota, Y.; Ozawa, N.; Nakanishi, H.; Kasai, H., Quantum States and Diffusion of Lithium Atom Motion on a Graphene. *J. Phys. Soc. Jpn.* **2009,** *79* (1), 014601.

33.   Prosini, P. P.; Lisi, M.; Zane, D.; Pasquali, M., Determination of the chemical diffusion coefficient of lithium in $LiFePO_4$. *Solid State Ion.* **2002,** *148* (1), 45-51.

34.   Kuwata, N.; Lu, X.; Miyazaki, T.; Iwai, Y.; Tanabe, T.; Kawamura, J., Lithium diffusion coefficient in amorphous lithium phosphate thin films measured by secondary ion mass spectroscopy with isotope exchange methods. *Solid State Ion.* **2016,** *294*, 59-66.

35.   Liu, W.; Shi, Q.; Qu, Q.; Gao, T.; Zhu, G.; Shao, J.; Zheng, H., Improved Li-ion diffusion and stability of a $LiNi_{0.5}Mn_{1.5}O_4$ cathode through in situ co-doping with dual-metal cations and incorporation of a superionic conductor. *J. Mater. Chem. A* **2017,** *5* (1), 145-154.

36.   (a) Fang, R.; Zhao, S.; Wang, D.-W.; Sun, Z.; Cheng, H.-M.; Li, F., Micro-Macroscopic Coupled Electrode Architecture for High-Energy-Density Lithium–Sulfur Batteries. *ACS Appl. Energy Mater.* **2019,** *2* (10), 7393-7402; (b) Hong, X.-J.; Tang, X.-Y.; Wei, Q.; Song, C.-L.; Wang, S.-Y.; Dong, R.-F.; Cai, Y.-P.; Si,

L.-P., Efficient Encapsulation of Small S_{2-4} Molecules in MOF-Derived Flowerlike Nitrogen-Doped Microporous Carbon Nanosheets for High-Performance Li–S Batteries. *ACS Appl. Mater. Interfaces* **2018,** *10* (11), 9435-9443.

37.   Meyer, B., Elemental sulfur. *Chem. Rev.* **1976,** *76* (3), 367-388.

38. Amin, R.; Chiang, Y.-M., Characterization of Electronic and Ionic Transport in $Li_{1-x}Ni_{0.33}Mn_{0.33}Co_{0.33}O_2$ (NMC333) and $Li_{1-x}Ni_{0.50}Mn_{0.20}Co_{0.30}O_2$ (NMC$_{523}$) as a Function of Li Content. *J. Electrochem. Soc.* **2016,** *163* (8), A1512-A1517.

39.   Di Stefano, D.; Miglio, A.; Robeyns, K.; Filinchuk, Y.; Lechartier, M.; Senyshyn, A.; Ishida, H.; Spannenberger, S.; Prutsch, D.; Lunghammer, S.; Rettenwander, D.; Wilkening, M.; Roling, B.; Kato, Y.; Hautier, G., Superionic Diffusion through Frustrated Energy Landscape. *Chem* **2019**.